Manuscript version: Author's Accepted Manuscript
The version presented in WRAP is the author's accepted manuscript and may differ from the published version or Version of Record.

Persistent WRAP URL:
http://wrap.warwick.ac.uk/168950

How to cite:
Please refer to published version for the most recent bibliographic citation information.
If a published version is known of, the repository item page linked to above, will contain details on accessing it.

Copyright and reuse:
The Warwick Research Archive Portal (WRAP) makes this work by researchers of the University of Warwick available open access under the following conditions.

Copyright © and all moral rights to the version of the paper presented here belong to the individual author(s) and/or other copyright owners. To the extent reasonable and practicable the material made available in WRAP has been checked for eligibility before being made available.

Copies of full items can be used for personal research or study, educational, or not-for-profit purposes without prior permission or charge. Provided that the authors, title and full bibliographic details are credited, a hyperlink and/or URL is given for the original metadata page and the content is not changed in any way.

Publisher's statement:
Please refer to the repository item page, publisher's statement section, for further information.

For more information, please contact the WRAP Team at: wrap@warwick.ac.uk.

warwick.ac.uk/lib-publications

The dynamic interplay of PIP_2 and ATP in the regulation of the K_{ATP} channel

Tanadet Pipatpolkai[1,2,3,4], Samuel G Usher[1,3,5,+], Natascia Vedovato[1,+], Frances M Ashcroft[1,*+], Phillip J Stansfeld[6,*+]

[1]Department of Physiology Anatomy and Genetics, Parks Road, Oxford, OX1 3PT, UK.
[2]Department of Biochemistry, South Parks Road, Oxford, OX1 3QU, UK.
[3]OXION Initiative in Ion Channels and Disease, University of Oxford, Oxford OX1 3PT, UK.
[4]Science for Life Laboratory, Department of Applied Physics, KTH Royal Institute of Technology, Tomtebodavägen 23, Solna, 17165, Sweden.
[5]Department of Drug Design and Pharmacology, University of Copenhagen, Jagtvej 160, 2100 Copenhagen, Denmark.
[6]School of Life Sciences & Department of Chemistry, University of Warwick, Coventry, CV4 7AL, UK.

*corresponding authors
[+]These authors contributed equally to the work

Keywords: ATP-sensitive potassium channel, molecular dynamics, phosphatidylinositol bisphosphate

Running Title: PIP_2 and ATP in the regulation of the K_{ATP} channel

Key Points

- The K_{ATP} channel is activated by the binding of phosphoinositol-bisphosphate (PIP_2) lipids and inactivated by the binding of adenosine triphosphate (ATP).
- K39 has the potential to bind to both PIP_2 and ATP. A mutation to this residue (K39R) results in neonatal diabetes.
- This study uses patch-clamp fluorometry, electrophysiology and molecular dynamics simulation.
- We show that PIP_2 competes with ATP for K39, and this reduces channel inhibition by ATP.
- We show that K39R increases channel affinity to PIP_2 by increasing the number of hydrogen bonds with PIP_2, when compared with the wild-type K39. This therefore decreases K_{ATP} channel inhibition by ATP.

Abstract

ATP-sensitive potassium (K_{ATP}) channels couple the intracellular ATP concentration to insulin secretion. K_{ATP} channel activity is inhibited by ATP binding to the Kir6.2 tetramer and activated by phosphatidylinositol-4,5-bisphosphate (PIP_2). Here, we use molecular dynamics (MD) simulation, electrophysiology and fluorescence spectroscopy to show that ATP and PIP_2 occupy different binding pockets that share a single amino acid residue, K39. When both ligands are present, simulations suggest that K39 shows a greater preference to co-ordinate with PIP_2 than ATP. They also predict that a neonatal diabetes mutation at K39 (K39R) increases the number of hydrogen bonds formed between K39 and PIP_2, potentially accounting for the reduced ATP inhibition observed in electrophysiological experiments. Our work suggests PIP_2 and ATP interact allosterically to regulate K_{ATP} channel activity.

123/150 words

Introduction

Pancreatic ATP-sensitive potassium (K_{ATP}) channels couple the metabolic state of the pancreatic beta-cell to insulin secretion (Rorsman & Ashcroft, 2018). Cryo-EM studies have provided high-resolution structures of the K_{ATP} channel complex. It comprises a central tetrameric pore formed from four inwardly rectifying potassium channel (Kir6.2) subunits, surrounded by four regulatory sulphonylurea receptor 1 (SUR1) subunits (Puljung, 2018). Binding of ATP to Kir6.2 closes the channel (Tucker *et al.*, 1997), whereas binding of phosphoinositides, such as phosphatidylinositol-4,5-bisphosphate (PIP_2), increases the channel open probability (Baukrowitz *et al.*, 1998). The ATP-binding site on Kir6.2 has been identified in several cryo-EM structures (Lee *et al.*, 2017*a*; Li *et al.*, 2017; Martin *et al.*, 2017*b*, 2017*a*; Wu *et al.*, 2018; Martin *et al.*, 2019; Ding *et al.*, 2019). The PIP_2 binding site has been resolved in structural studies of related Kir channels (Kir2.2, Kir3.2) (Hansen *et al.*, 2011; Whorton & MacKinnon, 2011) but not yet for Kir6.2. However, the structure of the Kir6.2 PIP_2 binding site has been previously predicted using site-directed mutagenesis, docking and coarse-grained molecular dynamics (CG-MD) simulation (Shyng *et al.*, 2000; Haider *et al.*, 2007; Stansfeld *et al.*, 2009; Pipatpolkai *et al.*, 2020*a*).

Mutations in the K_{ATP} channel lead to diseases of insulin secretion. Channel hyperactivation is associated with reduced insulin secretion and neonatal diabetes mellitus (NDM) whereas reduced channel activity leads to enhanced insulin secretion and congenital hyperinsulinism (CHI) (Ashcroft, 2005). Previous studies have shown that many NDM mutations cluster at the ATP-binding site, disrupting the ATP-sensitivity of the channel (Pipatpolkai *et al.*, 2020*b*). Some NDM mutations also interfere with PIP_2 regulation: for example, E179K enhances PIP_2 stimulation of the K_{ATP} current (as indicated by a reduction in neomycin block) and increases the predicted PIP_2 binding affinity (Pipatpolkai *et al.*, 2020*a*; De Franco *et al.*, 2020).

In addition to increasing the open probability of the K_{ATP} channel, PIP_2 binding to Kir6.2 reduces the inhibitory effect of ATP on the K_{ATP} current (Fan & Makielski, 1999). The precise mechanisms by which this phenomenon occurs have not been fully resolved. An increase in K_{ATP} channel open probability (P_{open}) leads to reduced ATP inhibition (Trapp *et al.*, 1998; Enkvetchakul *et al.*, 2000), and thus at least part of the effect of PIP_2 on ATP inhibition is mediated via changes in P_{open} (Enkvetchakul *et al.*, 2000). However, it has also been argued that PIP_2 may have an additional effect on ATP sensitivity that is independent of P_{open} (Enkvetchakul *et al.*, 2000). Both molecules carry similar negatively charged phosphate groups, and previous studies have proposed that PIP_2 competes with ATP for binding to the

C-terminus of Kir1.1 channels and competes with TNP-ATP binding to the C-terminus of Kir6.1 and Kir6.2 channels (MacGregor *et al.*, 2002). Comparison of recent structural studies of the channel with bound ATP, and docking and molecular dynamics simulations with PIP_2 suggest that ATP and PIP_2 have separate binding pockets (Haider *et al.*, 2005, 2007). Nevertheless, even if the two ligands do not share a binding pocket, it is still possible for ATP and PIP_2 to 'compete' for the same Kir6.2 subunit, described as 'negative heterotropic cooperativity' (Enkvetchakul *et al.*, 2001; Enkvetchakul & Nichols, 2003).

In this study, we used atomistic molecular dynamic simulations (AT-MD) to determine the dynamics of K39 when both ATP and PIP_2 occupy their respective binding sites. These data show that K39 can co-ordinate with both ATP and PIP_2, but with stronger preference to PIP_2 when both ligands are present. We used a combination of electrophysiology and fluorescence spectroscopy to assess how mutations which affect PIP_2 binding modulate ATP inhibition and nucleotide binding. These support the simulation findings and suggest how the mutations give rise to clinical disease.

Results

In this study, we used both atomistic molecular dynamic simulations and functional studies to explore the relationship between the ATP and PIP_2 binding sites of Kir6.2.

Simulation studies: exploring the PIP_2 and ATP binding sites on Kir6.2

We simulated the PIP_2 and ATP-binding sites in the Kir6.2 tetramer in the absence of SUR1 in order to exclude ATP interactions with SUR1. Previous simulations have shown there is no difference in the PIP_2 binding site when SUR1 is present (Pipatpolkai *et al.*, 2020*a*). In support of this observation, PIP_2 induces an increase in the P_{open} of Kir6.2 even in the absence of SUR1 (Fan & Makielski, 1999; Enkvetchakul *et al.*, 2000). Although the structure of the wild-type Kir6.2/SUR1 octameric complex has been resolved (Lee *et al.*, 2017*a*; Li *et al.*, 2017; Martin *et al.*, 2017*b*, 2017*a*; Wu *et al.*, 2018; Martin *et al.*, 2019; Ding *et al.*, 2019), there is no structure of Kir6.2 in either a PIP_2-bound or an ATP-bound conformation when SUR1 is absent. Thus, we built two atomistic simulation systems: Kir6.2 with ATP and Kir6.2 with PIP_2, and simulated each for 380 ns. To ensure that the initial protein structure was stable after converting to an atomistic system, we used pairwise root mean square deviation (RMSD) analysis over the last 300 ns of the simulation on the C_α atom of Kir6.2 as a measure of the stability of protein's tertiary structure. We observed that the C_α RMSD never deviated more than 4 Å across the trajectory in all simulation set-ups. Interestingly, the simulations with bound ligand (PIP_2 or ATP) showed slightly less C_α rearrangement than the apo state. This suggests that the 3D structure of the protein is highly stable throughout our simulation, and maybe further stabilised by the ligand (Figure 1A,B). To investigate the effect of PIP_2 and ATP binding on the local geometry of their binding sites, we selected amino acid residues within 4 Å of the ligand for > 40% of the time and defined them as contacting residues. Between the different Kir6.2 subunits, we found no significant difference in the contact that these residues made to either ATP or PIP_2 in the final 300 ns of the simulation. Thus, in all subsequent analyses, we defined each Kir6.2 subunit as a separate calculation to increase the sampling of an ATP molecule in the binding pocket. As there are 4 subunits and three separate simulations were run, this yielded a total of 12 data points per contacting residue. We found that in the last 300 ns of the simulation, the contacts made with the ligands were in good agreement with previous electrophysiological and computational studies (Figure 1A-D) (Shyng *et al.*, 2000; Haider *et al.*, 2007; Stansfeld *et al.*, 2009).

In the PIP_2 binding site, we found that R54 and K67 from one subunit, and R176 from an adjacent subunit co-ordinate with the 4’ phosphate of PIP_2, and that K39 co-ordinates with the 5’ phosphate (Figure 1A,B). Other uncharged residues (W68 and P69) that lie at the membrane-water interface also make strong contact with PIP_2. With the exception of P69, mutations at these residues have previously been shown to alter channel ATP sensitivity, increase the open probability and/or alter PIP_2 activation (Shyng *et al.*, 2000; Cukras *et al.*, 2002; Haider *et al.*, 2007; Männikkö *et al.*, 2011). By evaluating the root mean square fluctuation (RMSF) of all contact residues, we found that the binding of PIP_2 statistically reduces the dynamics of the K67 and R176 side chains (Figure 1E). However, only the difference at K67 showed biological significance (defined as a decrease of ~1 Å or more). These results agree well with previous coarse-grained simulations and hence, validate the co-ordination geometry of PIP_2 in its binding site (Stansfeld *et al.*, 2009; Pipatpolkai *et al.*, 2020*a*). Recently, the structure of an open state Kir6.2 channel with G334D and C166S mutations were solved (Zhao & MacKinnon, 2021). We conducted additional simulations to analyse the PIP_2 co-ordination geometry in the open state channel. These simulations suggest that there is no significance difference in the contact profile between the open and closed states of the channel (Figure 1F).

In the ATP-binding site, we found that R50 co-ordinates with both the β and the γ phosphate, K39 co-ordinates with the γ phosphate and K185 co-ordinates with the α and the β phosphate (Figure 1C,D). Both R50 and K185 dynamics were stabilised when ATP binds to the channel (Figure 1I). These findings agree with previous studies in which the ATP-binding residues in Kir6.2 were mapped using site-directed mutagenesis (Tucker *et al.*, 1998; Dabrowski *et al.*, 2004). Interestingly, the sidechain of K39 which is *ca.* 7 Å from the ATP molecule in the cryo-EM structure moves towards ATP and makes a contact in some simulations. All residues that contact ATP in the cryo-EM structure of the octameric Kir6.2/SUR1 complex (N48, I49, Q52, I182, F183, L205, Y330, S331, F333) also make contact in our simulations. These residues have been found to be crucial for ATP inhibition in functional studies (Tucker *et al.*, 1998). Mutations in residues that make contact with ATP also cause neonatal diabetes (Pipatpolkai *et al.*, 2020*b*).

Previous studies have highlighted the significance of SUR1 in ATP binding in Kir6.2 (Tucker *et al.*, 1997). We therefore conducted a short set of 100 ns simulations of the full K_{ATP} octameric complex. Here, we showed that the contacting residues between ATP and Kir6.2 remains unchanged in the presence of SUR1 (Figure 1D). However, we observed additional contacts between R202 (Occupancy = 0.89) and K205 (Occupancy = 0.44) in Kir6.2 with SUR1; in agreement with previous electrophysiological studies (Usher *et al.*, 2020). We also observed contacts between an ATP contacting residue, Q52, and SUR1 residues N131 and F132. Mutations at F132 to L and V are associated with developmental delay, epilepsy and neonatal diabetes (Ellard *et al.*, 2007; Rafiq *et al.*, 2008). This suggested potential residues where Kir6.2 may couple to SUR1 during the gating transitions.

The competition between PIP_2 and ATP for K39 co-ordination

Previous studies have shown that PIP_2 reduces channel ATP inhibition (Hilgemann & Ball, 1996; Baukrowitz *et al.*, 1998; Shyng & Nichols, 1998; Fan & Makielski, 1999). However, it was not clear if PIP_2 competes with ATP for the binding to Kir6.2 subunits or if it interferes with ATP-dependent gating (or both). Comparison of the cryo-EM structure of the ATP binding site with the predicted PIP_2 binding site suggest they lie *ca.* 25 Å from one another (Martin *et al.*, 2017*a*; Pipatpolkai *et al.*, 2020*a*). In our studies, K39 contacts both ATP and PIP_2 in independent simulations, but the position of the sidechain amine group is different. We next explored the dynamics of K39 when both ligands occupied their respective binding sites (Figure 3A). We calculated the distance between ATP or PIP_2 and the sidechain amine of K39. We observed that the position of K39 oscillated between co-ordination with ATP and PIP_2, but favoured PIP_2 more strongly (Figure 2A,B). Interestingly, a significant decrease ($P < 0.01$) in ATP contacts only occurred at residue K39 when PIP_2 was present (Figure 2C). This phenomenon is also observed using the quatrefoil structure of Kir6.2 (PDB ID: 6C3O) (Figure 2F,G). Therefore, we hypothesise that K39 may change its co-ordination from ATP to PIP_2 when both molecules are bound. The contact between K39 and PIP_2 remained unchanged in both in the presence and the absence of ATP (Figure 2D). Thus, we propose that the salt-bridges between K39 and ATP are broken in the presence of the PIP_2, causing the sidechain amine group on K39 to swing towards the PIP_2 headgroup.

With the exception of K39, no other residues in either the ATP- or PIP_2-binding site altered their contact probabilities, when both ligands were simultaneously present in their respective binding sites.

Computational and electrophysiological assessment of a neonatal diabetes mutation (K39R)

A mutation at K39 (K39R) is associated with transient neonatal diabetes (Zhang *et al.*, 2015). This substitution does not alter the charge of the side chain (as both lysine and arginine are positively charged), but an amine is replaced with a guanidium group. Given the results of our simulations, we would predict that this would result in an increased affinity for both PIP_2 and ATP. We simulated Kir6.2 containing the K39R substitution and compared the contacts between the guanidium group of the arginine and PIP_2 or ATP. In simulations with ATP alone, K39R spends more time in contact with ATP than the wild-type K39 (Figure 3A-C). In simulations with PIP_2 alone, residue 39 in both wild-type and K39R channels spent almost all of its time co-ordinating PIP_2. When both ATP and PIP_2 were present, we found that the contact probability of residue 39 with the PIP_2 headgroup was not significantly different in the either absence or the presence of the ATP (Figure 3D,E). We also observed that the presence of PIP_2 reduces the contacts between K39R and ATP, similar to the WT channel (Figure 3F,G). From this, we conclude that K39R mutation does not affect channel preference for PIP_2 in either the presence or the absence of ATP.

To quantify the strength of the interaction between PIP_2 and K39 or K39R, we carried out a hydrogen bond analysis to determine the number of H-bonds formed between the PIP_2 headgroup and the side chain of residue 39. Note that arginine can form up to 5 H-bonds spread over 3 amine groups, whereas lysine is only able to form a maximum of 3 bonds from a single amine. We observed that the guanidium group on the arginine forms two hydrogen bonds with the PIP_2 headgroup, whereas the lysine amine group forms only a single hydrogen bond. In both cases, the hydrogen bonds were formed with the 5' phosphate on the PIP_2 inositol headgroup both in the presence and absence of ATP (Figure 3D,E). This suggests that the K39R mutation enhances the strength of the interaction of residue 39 with PIP_2. We next calculated changes in an interaction between K39R and ATP. Here, we showed that K39R mutant is significantly more likely going to form two hydrogen bonds with ATP (Figure 3F). However, this phenomenon is abolished when PIP_2 is present (Figure 3G). Thus, we could propose that the binding of PIP_2 override the effect of channel inhibition by ATP both in WT and in K39R mutant. We postulate that this leads to reduced channel inhibition by ATP, and is the mechanism by which this mutation impairs insulin secretion and thereby leads to neonatal diabetes.

To explore this hypothesis functionally, we introduced three different substitutions at residue K39 (K39A, K39E, and K39R) into Kir6.2 and measured ATP inhibition of K_{ATP} currents in excised patches from HEK293T cells (Figure 4A). To facilitate identification of cells expressing the construct of interest, we attached GFP to the C-terminus of each Kir6.2 construct. We also co-transfected cells with SUR1 to allow assembly of fully octameric K_{ATP} channels. Kir6.2 with a C-terminal GFP tag, co-expressed with SUR1 (hereafter referred to as Kir6.2+SUR1), had an estimated IC_{50} value for ATP inhibition of 23.5 – 43.7 µM (95% intervals of the posterior probability distribution). We observed that substitution of K39 by either arginine (Kir6.2-K39R+SUR1) or glutamic acid (Kir6.2-K39E+SUR1) resulted in an increase in the estimated

IC_{50} value for ATP inhibition, while substitution by alanine (Kir6.2-K39A+SUR1) had no effect (Figure 4B,C).

The effect of substitutions at K39 on nucleotide binding assayed by patch-clamp fluorometry (PCF).

We next employed a recently described fluorimetric technique to directly measure nucleotide binding to the inhibitory binding site on Kir6.2 in the context of different amino acid substitutions at K39 (Puljung *et al.*, 2019; Usher *et al.*, 2020). Briefly, we introduced the fluorescent unnatural amino acid 3-(6-acetylnaphthalen-2-ylamino)-2-aminopropanoic acid (ANAP) at residue W311 of Kir6.2 with a C-terminal GFP tag (Kir6.2*). W311 was chosen as it is far away from ATP binding site and is unlikely to interfere with channel inhibition by TNP-ATP. We then measured Förster resonance energy transfer (FRET) between ANAP and a fluorescent analogue of ATP, trinitrophenyl-ATP (TNP-ATP), while simultaneously measuring inhibition of K_{ATP} currents (Figure 5A). In the absence of TNP-ATP, excised patches from HEK293T cells expressing Kir6.2*+SUR1 exhibited a fluorescence spectrum with two peaks; one at 470 nm corresponding to incorporated ANAP, and one at 510 nm corresponding to GFP. Application of TNP-ATP to excised patches resulted in a concentration-dependent inhibition of K_{ATP} currents and concomitant quenching of the ANAP fluorescence peak in each construct tested.

TNP-ATP inhibits K_{ATP} currents at lower concentrations than ATP for both Kir6.2+SUR1 and Kir6.2*-SUR1; the shift in nucleotide sensitivity was also similar for each of the mutants (A,E, and R) (Figure 6). As using this fluorescent analogue is necessary to directly measure binding to the Kir6.2 nucleotide-binding site, our findings therefore come with the caveat that measuring TNP-ATP binding may not directly reflect ATP binding to Kir6.2. As K_{ATP} channels are inhibited by a range of physiologically present nucleotides binding to Kir6.2 with different inhibitory strengths (Trapp *et al.*, 1997; Dabrowski *et al.*, 2003), we consider that our findings should be generalisable to other nucleotides.

As ANAP is site-specifically incorporated close to the Kir6.2 nucleotide-binding site, the observed fluorescence quenching is directly proportional to the extent of TNP-ATP binding to Kir6.2 (Usher *et al.*, 2020). We therefore fit the combined current inhibition and fluorescence quenching data to a simple three-parameter Monod-Wyman-Changeux (MWC)-type model (Figure 5B) to identify whether the changes in nucleotide inhibition we observe as a result of mutating K39 can be attributed to a particular biophysical parameter (Figure 5C,D). The three parameters the model includes are:

- L, which describes the equilibrium between the open and closed states of the channel pore,
- K_A, which is the affinity of nucleotides for the inhibitory binding site of Kir6.2,
- D, which represents the selective stabilisation of particular conformations of the channel by nucleotide binding, such that $D < 1$ promotes closure of the channel and $D > 1$ promotes opening of the channel.

The fits to the MWC-type model result in parameter estimates for L which are indistinguishable between Kir6.2*+SUR1 and the three K39 mutants, suggesting we were unable to detect any change in the open probability of the channel as a result of these substitutions. We observed reductions in the TNP-ATP binding affinity of each of the K39 mutants, although the posterior probability estimates of K_A for Kir6.2*+SUR1 and Kir6.2*-K39R+SUR1 overlap so this difference is not meaningful. In addition, fits to the Kir6.2*-K39E+SUR1 data yielded an estimate for D closer to 1 than that for Kir6.2*+SUR1, indicating a reduction in the selectivity of TNP-ATP for the closed state of the channel in this construct.

Discussion

Our work suggests a mechanistic explanation for how PIP_2 and ATP binding to Kir6.2 influence one another to modulate K_{ATP} channel activity. We show that the identity of the amino acid residue at position K39 is important for modulating the sensitivity of the channel to nucleotide inhibition, influencing both nucleotide binding affinity and the selectivity of nucleotides for the closed state.

Our atomistic MD simulations suggest that a single key residue, K39, forms part of both the ATP and PIP_2 binding sites on Kir6.2. When both ligands are present, K39 has a stronger preference for co-ordination with PIP_2 than with ATP (Figure 2C). No other residue (in either site) alters its contact probability in the presence of the other ligand. This finding is in support of previous experimental work which suggests that ATP and PIP_2 effectively compete for binding to a given Kir6.2 subunit (Enkvetchakul *et al.*, 2001; MacGregor *et al.*, 2002; Cukras *et al.*, 2002).

The simulation data further suggest that the K39R substitution in Kir6.2 which leads to transient neonatal diabetes (Zhang *et al.*, 2015) may lead to a gain-of-function phenotype by increasing the strength of the interaction of the side-chain with PIP_2 . In vitro, we would expect this to lead to an increase in PIP_2 affinity and a concomitant decrease in sensitivity of K_{ATP} channel currents to inhibition by nucleotides. Indeed, we observe that introducing the K39R mutation into Kir6.2 increases the IC_{50} for nucleotide inhibition by approximately 1.5-3-fold (Figure 5C), supporting this finding.

Curiously, however, we observed that substitution to K39E (with a negatively charged side-chain) also leads to a reduction in sensitivity to nucleotide inhibition, and substitution to K39A (no charge) does not affect inhibition at all. These findings are at odds with our hypothesis on the importance of hydrogen bonding at this residue. As our simulation data suggests K39 also coordinates ATP binding, we considered the possibility that we may be observing a mixture of effects on both ATP and PIP_2 regulation of the channel.

To disentangle these effects, we directly measured TNP-ATP binding to ANAP-labelled Kir6.2 constructs. Collecting binding data in parallel with current inhibition allows us to estimate the binding affinity of TNP-ATP for each of the Kir6.2*-K39 mutants (Figure 5C). These experiments suggest that the K39E substitution reduces the binding affinity of nucleotides, in addition to any effects it may have on PIP_2 coordination, explaining why we do not observe a lower IC_{50} for ATP inhibition of this construct. Unfortunately, while the IC_{50} for ATP inhibition of Kir6.2*-K39A+SUR1 was indistinguishable from the IC_{50} for ATP inhibition of Kir6.2*+SUR1 (Figure 4C), we observed a noticeable difference between current inhibition of the two constructs by TNP-ATP, making it difficult to interpret our findings for this mutant.

In summary, we propose that residue K39 of Kir6.2 can coordinate either ATP or PIP_2 binding – but not both – in support of previous work (Figure 7). Mutation of this residue to arginine results in neonatal diabetes, which we suggest occurs by enhancing the strength of the PIP_2 interaction with the side-chain, resulting in a loss of sensitivity to inhibition by nucleotides.

Materials and methods

Coarse-Grained system preparation

We used four molecular complexes in our simulations: (i) the human Kir6.2 model from residue 32 to 352 without SUR1 in the propeller conformation (PDB entry: 6BAA) (Martin *et al.*, 2017*a*), (ii) the Kir6.2 model in quatrefoil conformation (PDB entry: 6C3O) (Lee *et al.*, 2017*b*), (iii) an open state Kir6.2 channel with mutation on G334D and C166S (PDB entry: 7S5T), and (iv) a full K_{ATP} propeller channel octameric complex comprising of four copies of Kir6.2 (residues 32-352) and four copies of SUR1. These complexes were converted to a coarse-grained representation using *martinize.py*, embedded in the palmitoyl-oleoyl-phosphatidylcholine (POPC) bilayer and solvated in water and 0.15 M NaCl using a self-assembly MemProtMD pipeline (Stansfeld *et al.*, 2015)(https://github.com/pstansfeld/MemProtMD/). All simulations were carried out using the Martini v2.2 biomolecular forcefield (Marrink *et al.*, 2007; Monticelli *et al.*, 2008). The tertiary and quaternary structures of the protein were maintained through the application of an elastic network with a force constant of 1,000 kJ/mol/nm^2 between two coarse-grained backbone particles within 0.5-0.9 nm. A temperature of 323 K was maintained with V-rescale temperature coupling (Bussi *et al.*, 2007), while 1 bar pressure was controlled using semi-isotropic Parrinello-Rahman pressure coupling (Parrinello & Rahman, 1981). The position of the coarse-grained PIP_2 is taken from the chicken Kir2.2-PIP_2:diC8 after conversion to a coarse-grained model (Hansen *et al.*, 2011). Systems were energy minimised using the steepest descents algorithm and equilibrated for 1 µs. All simulations were carried out using GROMACS-2019.4 (Van Der Spoel *et al.*, 2005).

Atomistic simulation set up

The coarse-grained simulation system (Kir6.2, lipids - PIP_2 and POPC, ions and water) was converted to atomistic using the CG2AT pipeline (Stansfeld & Sansom, 2011). The K39R mutant model was generated using PyMOL with the minimum initial stearic clashes (Schrodinger LLC, 2015). The exact position of the ATP molecule was taken from the cryo-EM structure (PDB entry: 6BAA) and placed in the Kir6.2 ATP binding site. The initial position of the hydrogen atoms was added using PyMOL. All simulations were carried out using CHARMM36m biomolecular forcefield with the virtual sites on the proteins and lipids CH_3 and NH_3^+ groups, allowing the integration timestep of 4 fs in the production run (Huang *et al.*, 2017; Olesen *et al.*, 2018). The forcefield for the ATP molecule was derived from the CHARMM-GUI (Kim *et al.*, 2017). In this study, 4 different conditions were set (Apo, ATP-bound, PIP_2-bound, both ATP and PIP_2 bound) and simulations were carried out for 3 repeats.

The systems were energy minimised using the steepest descents algorithm with non-hydrogen atoms restrained at 1000 kJ/mol/nm^2. This was then followed by a 5 ns equilibration for the system where the C_α backbone on the protein and the non-hydrogen atoms on the ATP molecules were restrained with 1000 kJ/mol/nm^2 with 4 fs timesteps. A temperature of 310 K was maintained with V-rescale temperature coupling (Bussi *et al.*, 2007), while 1 atm pressure was controlled using semi-isotropic Parrinello-Rahman pressure coupling (Parrinello & Rahman, 1981). The simulation was then further equilibrated with only C_α restraint on the protein for another 15 ns in similar conditions. Then three repeats of the 380 ns production runs were implemented, in which the first 80 ns of the simulations were discarded as equilibration. All simulations, H-bond calculations and distance calculation were calculated using GROMACS-2019.4 (Abraham *et al.*, 2015). We used MDAnalysis to calculate pairwise RMSD to define change in protein dynamics across the trajectory (Theobald, 2005; Beckstein *et al.*, 2009; Michaud-Agrawal *et al.*, 2011; Gowers *et al.*, 2016).

Molecular biology

Human Kir6.2 and SUR1 were subcloned into pCGFP_EU (GFP-tagged constructs) and pcDNA4/TO, respectively. Site-directed mutagenesis and amber stop codons were introduced using the QuikChange XL system (Stratagene; San Diego, CA), and verified by sequencing (DNA Sequencing and Services; Dundee, Scotland), as previously described (Usher *et al.*, 2020). HEK-293T cells were grown in in Dulbecco's Modified Eagle Medium (DMEM, Sigma) with the addition of 10% fetal bovine serum, 100 U/mL penicillin, and 100 μg/mL streptomycin (Thermo Fisher Scientific; Waltham, MA) at 37°C, 5%/95% CO_2/air. Cells were seeded in T25 flasks 24 hours, before transfection with TransIT-LT1 (Mirus Bio LLC; Madison, WI). Protein expression and trafficking to the plasma membrane were optimized by including 300 μM tolbutamide in the transfection media (Yan *et al.*, 2007). ANAP-tagged Kir6.2 constructs were cultured in the presence of 20 μM ANAP (free acid, AsisChem; Waltham, MA) and 48 hours post-transfection, cells were re-plated onto either poly-D-lysine coated glass-bottomed FluoroDishes (FD35-PDL-100, World Precision Instruments) or poly-L-lysine coated 35 mm petri dishes (Corning). pCDNA4/TO and pANAP were obtained from Addgene. peRF1-E55D (*Homo sapiens*) and pCGFP_EU (*Aequorea victoria*) were kind gifts from the Chin Laboratory (MRC Laboratory of Molecular Biology, Cambridge UK) and Gouaux Laboratory (Vollum Institute, Portland OR USA), respectively.

Electrophysiology

Extracellular (pipette) solutions contained (in mM) 140 KCl, 1 EGTA, 10 HEPES (pH 7.3 with KOH). The intracellular (bath) solutions contained (in mM) 140 KCl, 1 EDTA, 1 EGTA, 10 HEPES (pH 7.3 with KOH). Inside-out patches were excised from transfected HEK293T cells using borosilicate glass pipettes (GC150F-15, Harvard Apparatus; Holliston, MA) pulled to a resistance of 1-3 MΩ. Data were acquired at a holding potential of -60 mV using an Axopatch 200B amplifier and a Digidata 1322A digitizer run through pClamp 9 software (Molecular Devices; San Jose, CA). Currents were low-pass filtered at 1-5 kHz and digitized at 10-20 kHz.

Patches were perfused with an 8-channel µFlow or a manual gravity perfusion system. Different concentrations of adenosine triphosphate (ATP, Sigma) or fluorescent trinitrophenyl adenosine triphosphate (TNP-ATP, Jena Bioscience) were added to the bath solution to assess current inhibition and/or nucleotide binding. Nucleotide-induced inhibition was corrected for rundown by alternating test concentrations of nucleotide solution with nucleotide-free solution. The inhibition was expressed as a fraction of the control currents before and after the test solution as described previously (Proks *et al.*, 2010). For experiments with TNP-ATP, the zero current level was determined by perfusing 10 mM $BaCl_2$ at the end of each recording at a holding potential of +60 mV. Current inhibition data were fitted with the following Hill equation:

$$\frac{I}{I_{max}} = 1 - I_{max} + \frac{I_{max}}{1 + 10^{(IC_{50} - [nucleotide]) \cdot -h}}$$

Fitting was performed with the *brms* (Bayesian Regression Models using 'Stan') package in R as a mixed-effects model (Bürkner, 2017) with the IC_{50} value allowed to vary between individual excised patches. Prior probability distributions were supplied for each parameter as follows:

$$h \sim Normal(\mu : 1, \sigma^2 : 0.3)$$
$$I_{max} \sim Uniform(min : 0, max : 1)$$
$$IC_{50} \sim Normal(\mu : -4, \sigma^2 : 1)$$

Each model was run across 4 chains for 4,000 iterations including a burn-in period of 2,000 iterations for a total of 8,000 samples. Each model parameter achieved a minimum effective sample size of 5,000 and a potential scale reduction statistic ($\hat{R}$) of 1.00. Contrasts were calculated by subtracting the full posterior probability for the IC_{50} of the 'control' construct from each compared mutant channel. The resulting probability distribution represents the estimated fold-change in IC_{50} (as the estimated IC_{50} is expressed as a log value) resulting from making the indicated mutation.

Fluorescence measurements

Fluorescence spectra from excised patches were collected and analysed as described previously (Usher *et al.*, 2020). Briefly, the tip of the patch pipette was centred on the slit of the spectrometer immediately after patch excision. ANAP was excited using a 385 nm LED source (ThorLabs; Newton, NJ) with a 390/18 nm band-pass excitation filter, after which the emitted light passed through a 400 nm long-pass emission filter (ThorLabs) and an IsoPlane 160 Spectrometer (Princeton Instruments; Trenton, NJ) with a 300 grooves mm^{-1} grating. Images were collected with 1 s exposures on a Pixis 400BR_eXcelon CCD (Princeton Instruments). Spectra were corrected for background fluorescence, then ANAP intensity was calculated by averaging the fluorescence intensity measured between 469.5 nm and 474.5 nm. This intensity was corrected for bleaching with a single exponential decay.

Statistics and data presentation

Concentration-response data are plotted with each measurement shown as a data point. The Hill equation fits for nucleotide inhibition are displayed as the median fit (solid line) and the 95% intervals (shaded area) of the posterior probability distribution. The MWC-type model fits are also displayed as the median fit (solid line) and the 95% intervals (shaded area) of the posterior probability distribution. Where posterior probability distributions for parameter values are shown, they are displayed with the 50%, 80% and 95% intervals of the distribution in progressively lighter shades of colour.

Monod-Wyman-Changeux model fitting

The MWC-type model fitted here is described by the following sets of equations:

$$\frac{F}{F_{max}} = \frac{K_A[TNP-ATP]\cdot(1 + K_A[TNP-ATP])^3 + LDK_A[TNP-ATP]\cdot(1 + DK_A[TNP-ATP])^3}{(1 + K_A[TNP-ATP])^4 + L(1 + DK_A[TNP-ATP])^4}$$

$$\frac{I}{I_{max}} = \frac{L(1 + DK_A[TNP-ATP])^4}{(1 + K_A[TNP-ATP])^4 + L(1 + DK_A[TNP-ATP])^4}\cdot\frac{1 + L}{L}$$

The full rationale behind this model choice is described in more detail previously (Puljung *et al.*, 2019; Usher *et al.*, 2020). Briefly, in this model, *L* represents an equilibrium constant where the K_{ATP} open probability (P_{open}) is equal to *L*/(*L*+*1*), reflecting the ability of K_{ATP} to open and close in the absence of nucleotides. Each ligand binding event (K_A) is independent and each bound ligand favours the closed state by the same factor (*D*). This model is fit to the combined current inhibition and fluorescence quenching data using the *brms* package in R (Bürkner, 2017). Prior probability distributions were supplied for each parameter as follows:

$$log_{10}(L) \sim Normal(\mu : 0, \sigma^2 : 0.7)$$
$$log_{10}(K_A) \sim Uniform(min : 2, max : 6)$$
$$D \sim Uniform(min : 0, max : 1)$$

The model was run across 4 chains for 4,000 iterations including a burn-in period of 2,000 iterations for a total of 8,000 samples. Each model parameter achieved a minimum effective sample size of 5,000 and a potential scale reduction statistic ($\hat{R}$) of 1.00.

Data availability statement

All data in a non-identifying format are securely stored at the Universities of Oxford and Warwick, UK. The data are available upon request.

Acknowledgements

We thank Michael C. Puljung for discussions about the MWC modelling and interpretations of the parameters. We also thank Irfan Alibay, Robin Corey, Michael Horrell, Raul Terron-Exposito, and Owen Vickery for advice and technical support.

Author contributions

T.P. performed the coarse-grained and atomistic molecular dynamics simulations. N.V. and S.U. performed the molecular biology, electrophysiology and fluorescence measurements. All authors jointly designed the experiments, analysed the data and wrote the manuscript.

Competing interests

The authors declare no competing interests.

Funding

T.P. and S.U. holds a Wellcome Trust OXION studentship. T.P. holds a Clarendon scholarship. Research in PJS's lab is funded by Wellcome (208361/Z/17/Z), the MRC (MR/S009213/1) and BBSRC (BB/P01948X/1, BB/R002517/1 and BB/S003339/1). Research in FMA's lab is funded by the MRC (MR/T002107/1) and BBSRC (BB/R002517/1, BB/R017220/1). This project made use of time on ARCHER and JADE granted via the UK High-End Computing Consortium for Biomolecular Simulation, HECBioSim (http://hecbiosim.ac.uk), supported by EPSRC (grant no. EP/R029407/1).

Figures and figure legends

Figure 1. PIP_2 binding sites

(A) The structure of the Kir6.2 tetramer shown with four PIP_2 molecules in their binding sites. Inset: Interactions between PIP_2 (bronze) and basic residues in two chains of Kir6.2 (yellow and green). (B) The fraction of time that the indicated residues are in < 4Å proximity to PIP_2 during the final 300 ns of the simulations (defined as “PIP_2 occupancy”). (C) The structure of the Kir6.2 tetramer shown with four ATP molecules in their binding site. Inset: Interactions between ATP (CPK) and basic residues in two chains of Kir6.2 (yellow and green) after a 380 ns simulation. (D) The fraction of time that the indicated residues are in < 4 Å proximity to ATP during the final 300 ns of the simulations (defined as “ATP occupancy”). (E) Root mean square fluctuation (RMSF) analysis of the residues on the Kir6.2 tetramer, which contact the PIP_2 molecule in the absence (blue) and the presence (red) of PIP_2. (F) The fraction of time that the indicated residues are in < 4Å proximity to PIP_2 (defined as “PIP_2 occupancy”) during the final 300 ns of the simulations of the C166S/G334D structure that was captured in an ‘open-state’. (G) The fraction of time that the indicated residues on SUR1 which are in < 4Å proximity to ATP (defined as “ATP occupancy”) collected during 100 ns of the simulation for Kir6.2+SUR1 simulation (blue). (H) The fraction of time that the indicated residues on SUR1 which are in < 4Å proximity to Q52 on Kir6.2 (defined as “Q52 contact”) collected during 100 ns of the simulation for Kir6.2+SUR1 simulation (blue). (I) Root mean square fluctuation (RMSF) analysis of the residues on the Kir6.2 tetramer, which contact the ATP molecule in the absence (blue) and the presence (red) of ATP. For each plot three simulations were run, and each subunit of the tetramer is treated as an individual data point (which makes a total of 12 data points). For each occupancy datapoint only residues with greater than 0.4 occupancy are shown. The error bar indicates the 95% confidence interval around the mean. ** $P < 0.01$ (Student’s t-test).

Figure 2. Changes in the ATP and PIP_2 binding sites when both ligands are present
(A) Interactions between Kir6.2 (two chains are indicated in yellow and green), ATP (grey CPK colouring) and the PIP_2 (bronze) headgroup. Only the basic residues of the protein are shown. (B) A representative trace showing the distance calculation between K39 and ATP (black) and K39 and PIP_2 (red) across a single 300 ns trajectory. The darker lines show running averages of every 1 ns of the simulation. (C) The fraction of time that the residues are in < 4 Å proximity to ATP during the final 300 ns of the simulations (defined as “ATP occupancy”) in the absence (black) and presence (red) of PIP_2. (D) The fraction of time that the residues are in < 4Å proximity to PIP_2 during the final 300 ns of the simulations (defined as “PIP_2 occupancy”) in the absence (black) and presence (red) of ATP. (E) The fraction of time that K39 on Kir6.2 which are in < 4Å proximity to ATP (defined as “ATP occupancy”) in the presence and absence of PIP_2. (F) The fraction of time that K39 on Kir6.2 which are in < 4Å proximity to ATP (defined as “ATP occupancy”) in the quatrefoil and propeller Kir6.2 structures. Only residues where the mean occupancy is greater than 0.4 are plotted. Three simulations were run, and each subunit of the tetramer is treated as an individual data point (which makes a total of 12 data points). The error bar indicates the 95% confidence interval around the mean. The asterisks indicate the significant difference at $P < 0.01$ using the Student’s t-test.

Figure 3. The K39R mutation changes the PIP_2 binding configuration

The fraction of time that the K39 or K39R are in < 4 Å proximity to either ATP or PIP_2 during the final 300 ns of the simulations. (A) The PIP_2 occupancy in the absence and presence of ATP. (B) The ATP occupancy in the absence and presence of PIP_2. (C) The fraction of time that K39 (or K39R) residues are in < 4Å proximity to ATP during the final 300 ns of the simulations (defined as "ATP occupancy") when both ATP and PIP_2 are present. (D-G) Hydrogen bond analysis showing the fraction of time when K39 (red) or K39R (blue) forms a different number of H-bonds with the PIP_2 headgroup during the final 300 ns of the simulations in the (D) absence and (E) presence of ATP. Also shown is the number of H-bonds with ATP during the final 300 ns of the simulations in the (F) absence and (G) presence of PIP_2. In all analysis, there are three simulations, and each subunit of a tetramer is being treated as an individual data point (a total of n = 12). The error bar indicates the 95% confidence interval around the mean. ** $P < 0.01$ (Student's t-test).

Figure 4. Substitutions at K39 alter ATP inhibition of K_{ATP} channels.

(A) ATP concentration-response curves recorded from inside-out patches excised from HEK293T cells co-expressing the indicated GFP-tagged Kir6.2 construct and SUR1. Each data point is a single measurement, normalized to the maximum current observed in that patch. The fits are to the Hill equation specified in the Methods, with the solid line representing the median fit and the shaded area the 95% interval of the posterior probability distribution. The fit for Kir6.2+SUR1 is shown in grey in each panel to facilitate comparison. Parameters for each fit are given in in Table 1. A representative current trace showing a typical response to application of 100 µM ATP is shown above to each concentration-response plot. The zero-current level is shown as a dotted line. (B) Posterior probability distributions for the IC_{50} parameters estimated from the Hill fits shown in panel A. The progressively lighter shades of colour represent the 50%, 80% and 95% intervals of the distribution. There is a 95% probability that the true IC_{50} value for each construct is located within the lightest coloured interval. The IC_{50} estimates for each patch are shown as filled circles. (C) Fold change between the indicated IC_{50} value for ATP inhibition of control Kir6.2+SUR1 currents (indicated by the vertical line at 1.0) and that of the indicated mutant channel. Same colour code as in B.

Figure 5. Substitutions at K39 alter nucleotide binding to Kir6.2.

(A) Representative current (left) and fluorescence (right) traces for Kir6.2*+SUR1 (top) and Kir6.2*-K39R+SUR1 (bottom). The coloured regions of the current traces indicate application of TNP-ATP, with concentrations given in M. The correspondingly coloured spectral traces were captured simultaneously with the current recordings. The light blue region indicated in the fluorescence traces indicates the fluorescence peak corresponding to ANAP, and the light green region that corresponding to GFP. The dotted lines indicate the zero-current levels, and the background fluorescence levels. (B) Concentration-response curves for current inhibition (filled data points) and fluorescence quenching (open data points) for the indicated channels. Each data point is a single measurement, normalized to the maximum current or fluorescence observed in that patch. Fluorescence measurements have been further corrected to account for fluorescence bleaching and crosstalk as described in the Methods. The fits are to the MWC equation specified in the Methods, with the solid line representing the median fit and the shaded area the 95% interval of the posterior probability distribution. The fits for Kir6.2*+SUR1 are shown in grey in each panel to facilitate comparison. (C) Schematic of the MWC-type model used to model the regulation of the K_{ATP} channel by nucleotide binding to Kir6.2. The three equilibrium parameters used to fit our observed data (L, K_A, and D) are shown in bold. Their definitions are given in the main text. (D) Posterior probability distributions for each of the three parameters estimated in the MWC fits shown in panel B. The progressively lighter shades of colour represent the 50%, 80% and 95% intervals of the distribution. The probability that the true parameter value of each construct is located within the lightest coloured interval is 95%.

Figure 6. Substitutions at K39 alter TNP-ATP inhibition of K_{ATP} channels.

(A) TNP-ATP concentration-response curves recorded from inside-out patches excised from HEK293T cells co-expressing the indicated GFP-tagged Kir6.2 construct and SUR1. Each data point is a single measurement, normalized to the maximum current observed in that patch. The fits are to the Hill equation specified in the Methods, with the solid line representing the median fit and the shaded area the 95% interval of the posterior probability distribution. The fit for Kir6.2+SUR1 is shown in grey in each panel to facilitate comparison. Parameters for each fit are given in Table 2. (B) ATP concentration-response curves recorded from inside-out patches excised from HEK293T cells co-expressing the indicated GFP-tagged Kir6.2* construct and SUR1. Data are presented and analysed as in panel A, and parameters for each fit are given in Table 3. (C) Posterior probability distributions of the fold-change between the IC_{50} value for TNP-ATP inhibition of control Kir6.2+SUR1 currents (indicated by the vertical line at 1.0) and that of the indicated mutant channel. The progressively lighter shades of colour represent the 50%, 80% and 95% intervals of the distribution. The probability that the true fold-change in IC_{50} for each construct is located within the lightest coloured interval is 95%. (D) Posterior probability distributions of the fold-change between the IC_{50} value for ATP inhibition of control Kir6.2*+SUR1 currents and that of the indicated mutant channel. Colour scheme as in panel C.

Figure 7. Schematic representation of the interaction between Kir6.2, ATP and PIP$_2$

Interaction between ATP (silver sphere), PIP$_2$ (hexagon with silver phosphate group – P) and Kir6.2 (green). A positive charge on K39 is denoted in yellow (or red in the K39R mutant). The orange dashed line represents hydrogen bonds between K39 and the ligand. The arrow represents the change in motion of K39.

Construct	95% lower quantile (μM)	95% upper quantile (μM)	Median (μM)	N
Kir6.2	94.1	455	215	5
Kir6.2+SUR1	24.5	43.7	32.7	8
Kir6.2-K39A+SUR1	23.7	36.2	29.2	7
Kir6.2-K39E+SUR1	42.7	83.0	59.2	6
Kir6.2-K39R	159	762	370	3
Kir6.2-K39R+SUR1	53.6	97.8	72.1	6

Table 1. Inhibition of Kir6.2 constructs by ATP.

Fitted parameters for the Hill fits to dose-response curves shown in Figure 4. Fitting was performed as described in the Methods. Each N is a single inside-out patch from which a complete dose-response has been measured.

Construct	95% lower quantile (μM)	95% upper quantile (μM)	Median (μM)	N
Kir6.2+SUR1	0.70	1.74	1.08	13
Kir6.2-K39A+SUR1	7.06	17.0	11.0	9
Kir6.2-K39E+SUR1	4.20	39.7	11.8	5
Kir6.2-K39R+SUR1	1.50	4.17	2.48	9

Table 2. Inhibition of Kir6.2 constructs by TNP-ATP.

Fitted parameters for the Hill fits to dose-response curves shown in Figure 6A,C. Fitting was performed as described in the Methods. Each N is a single inside-out patch from which a complete dose-response has been measured.

Construct	95% lower quantile (µM)	95% upper quantile (µM)	Median (µM)	N
Kir6.2*+SUR1	79.6	97.7	119	11
Kir6.2*-K39A+SUR1	109	157	226	7
Kir6.2*-K39E+SUR1	101	154	234	7
Kir6.2*-K39R+SUR1	308	412	547	8

Table 3. Inhibition of Kir6.2* constructs by ATP.

Fitted parameters for the Hill fits to dose-response curves shown in Figure 6B,D. Fitting was performed as described in the Methods. Each N is a single inside-out patch from which a complete dose-response has been measured.

Reference

Abraham MJ, Murtola T, Schulz R, Páll S, Smith JC, Hess B & Lindah E (2015). Gromacs: High performance molecular simulations through multi-level parallelism from laptops to supercomputers. *SoftwareX* **1–2,** 19–25.

Ashcroft FM (2005). ATP-sensitive potassium channelopathies: Focus on insulin secretion. *J Clin Invest* **115,** 2047–2058.

Baukrowitz T, Schulte U, Oliver D, Herlitze S, Krauter T, Tucker SJ, Ruppersberg JP & Fakler B (1998). PIP2 and PIP as determinants for ATP inhibition of KATP channels. *Science (80-)* **282,** 1141–1144.

Beckstein O, Denning EJ, Perilla JR & Woolf TB (2009). Zipping and Unzipping of Adenylate Kinase: Atomistic Insights into the Ensemble of Open↔Closed Transitions. *J Mol Biol* **394,** 160–176.

Bründl M, Pellikan S & Stary-Weinzinger A (2021). Simulating PIP(2)-Induced Gating Transitions in Kir6.2 Channels. *Front Mol Biosci* **8,** 711975.

Bürkner P-C (2017). brms: An R Package for Bayesian Multilevel Models Using Stan. *J Stat Software, Artic* **80,** 1–28.

Bussi G, Donadio D & Parrinello M (2007). Canonical sampling through velocity rescaling. *J Chem Phys* **126,** 14101.

Cukras CA, Jeliazkova I & Nichols CG (2002). The role of NH2-terminal positive charges in the activity of inward rectifier KATP channels. *J Gen Physiol* **120,** 437–446.

Dabrowski M, Tarasov A & Ashcroft FM (2004). Mapping the architecture of the ATP-binding site of the KATPchannel subunit Kir6.2. *J Physiol* **557,** 347–354.

Dabrowski M, Trapp S & Ashcroft FM (2003). Pyridine nucleotide regulation of the KATP channel Kir6.2/SUR1 expressed in Xenopus oocytes. *JPhysiol* **550,** 357–363.

Ding D, Wang M, Wu J-X, Kang Y & Chen L (2019). The Structural Basis for the Binding of Repaglinide to the Pancreatic K_{ATP} Channel. *Cell Rep* **27,** 1848-1857.e4.

Ellard S, Flanagan SE, Girard CA, Patch A-M, Harries LW, Parrish A, Edghill EL, Mackay DJG, Proks P, Shimomura K, Haberland H, Carson DJ, Shield JPH, Hattersley AT & Ashcroft FM (2007). Permanent neonatal diabetes caused by dominant, recessive, or compound heterozygous SUR1 mutations with opposite functional effects. *Am J Hum Genet* **81,** 375–382.

Enkvetchakul D, Loussouarn G, Makhina E & Nichols CG (2001). ATP interaction with the open state of the KATP channel. *Biophys J* **80,** 719–728.

Enkvetchakul D, Loussouarn G, Makhina E, Shyng SL & Nichols CG (2000). The kinetic and physical basis of K(ATP) channel gating: toward a unified molecular understanding.

Biophys J **78,** 2334–2348.

Enkvetchakul D & Nichols CG (2003). Gating Mechanism of KATP Channels. *J Gen Physiol* **122,** 471 LP – 480.

Fan Z & Makielski JC (1999). Phosphoinositides decrease ATP sensitivity of the cardiac ATP-sensitive K(+) channel. A molecular probe for the mechanism of ATP-sensitive inhibition. *J Gen Physiol* **114,** 251–269.

De Franco E et al. (2020). Update of variants identified in the pancreatic β-cell KATP channel genes KCNJ11 and ABCC8 in individuals with congenital hyperinsulinism and diabetes. *Hum Mutat* **41,** 884–905.

Gowers RJ, Linke M, Barnoud J, Reddy TJE, Melo MN, Seyler SL, Domański J, Dotson DL, Buchoux S, Kenney IM & Beckstein O (2016). MDAnalysis: A Python Package for the Rapid Analysis of Molecular Dynamics Simulations. *Proc 15th Python Sci Conf*98–105.

Haider S, Antcliff JF, Proks P, Sansom MSP & Ashcroft FM (2005). Focus on Kir6.2: A key component of the ATP-sensitive potassium channel. *J Mol Cell Cardiol* **38,** 927–936.

Haider S, Tarasov AI, Craig TJ, Sansom MSP & Ashcroft FM (2007). Identification of the PIP2-binding site on Kir6.2 by molecular modelling and functional analysis. *EMBO J* **26,** 3749–3759.

Hansen SB, Tao X & MacKinnon R (2011). Structural basis of PIP2 activation of the classical inward rectifier K+ channel Kir2.2. *Nature* **477,** 495–498.

Hilgemann DW & Ball R (1996). Regulation of Cardiac Na+/Ca2+ Exchange and KATP Potassium Channels by PIP2. *Science (80-)* **273,** 956 LP – 959.

Huang J, Rauscher S, Nawrocki G, Ran T, Feig M, de Groot BL, Grubmüller H & MacKerell AD (2017). CHARMM36m: an improved force field for folded and intrinsically disordered proteins. *Nat Methods* **14,** 71–73.

Kim S, Lee J, Jo S, Brooks III CL, Lee HS & Im W (2017). CHARMM-GUI ligand reader and modeler for CHARMM force field generation of small molecules. *J Comput Chem* **38,** 1879–1886.

Lee KPK, Chen J & Mackinnon R (2017*a*). Molecular structure of human katp in complex with ATP and ADP. *Elife*; DOI: 10.7554/eLife.32481.

Lee KPK, Chen J & MacKinnon R (2017*b*). Molecular structure of human KATP in complex with ATP and ADP ed. Swartz KJ. *Elife* **6,** e32481.

Li N, Wu JX, Ding D, Cheng J, Gao N & Chen L (2017). Structure of a Pancreatic ATP-Sensitive Potassium Channel. *Cell* **168,** 101-110.e10.

MacGregor GG, Dong K, Vanoye CG, Tang L, Giebisch G & Hebert SC (2002). Nucleotides and phospholipids compete for binding to the C terminus of KATP channels. *Proc Natl Acad Sci* **99,** 2726 LP – 2731.

Männikkö R, Stansfeld PJ, Ashcroft AS, Hattersley AT, Sansom MSP, Ellard S & Ashcroft

FM (2011). A conserved tryptophan at the membrane-water interface acts as a gatekeeper for Kir6.2/SUR1 channels and causes neonatal diabetes when mutated. *J Physiol* **589,** 3071–3083.

Marrink SJ, Risselada HJ, Yefimov S, Tieleman DP & de Vries AH (2007). The MARTINI Force Field: Coarse Grained Model for Biomolecular Simulations. *J Phys Chem B* **111,** 7812–7824.

Martin GM, Kandasamy B, DiMaio F, Yoshioka C & Shyng S-L (2017*a*). Anti-diabetic drug binding site in a mammalian KATP channel revealed by Cryo-EM ed. Swartz KJ. *Elife* **6,** e31054.

Martin GM, Sung MW, Yang Z, Innes LM, Kandasamy B, David LL, Yoshioka C & Shyng S-L (2019). Mechanism of pharmacochaperoning in a mammalian KATP channel revealed by cryo-EM ed. Aldrich R, Yellen G, Moiseenkova-Bell VY, Nichols CG & Agar J. *Elife* **8,** e46417.

Martin GM, Yoshioka C, Rex EA, Fay JF, Xie Q, Whorton MR, Chen JZ & Shyng SL (2017*b*). Cryo-EM structure of the ATP-sensitive potassium channel illuminates mechanisms of assembly and gating. *Elife*; DOI: 10.7554/eLife.24149.

Michaud-Agrawal N, Denning EJ, Woolf TB & Beckstein O (2011). MDAnalysis: A toolkit for the analysis of molecular dynamics simulations. *J Comput Chem* **32,** 2319–2327.

Monticelli L, Kandasamy SK, Periole X, Larson RG, Tieleman DP & Marrink S-J (2008). The MARTINI Coarse-Grained Force Field: Extension to Proteins. *J Chem Theory Comput* **4,** 819.

Olesen K, Awasthi N, Bruhn DS, Pezeshkian W & Khandelia H (2018). Faster Simulations with a 5 fs Time Step for Lipids in the CHARMM Force Field. *J Chem Theory Comput*; DOI: 10.1021/acs.jctc.8b00267.

Parrinello M & Rahman A (1981). Polymorphic transitions in single crystals: A new molecular dynamics method. *J Appl Phys* **52,** 7182–7190.

Pipatpolkai T, Corey RA, Proks P, Ashcroft FM & Stansfeld PJ (2020*a*). Evaluating inositol phospholipid interactions with inward rectifier potassium channels and characterising their role in disease. *Commun Chem* **3,** 147.

Pipatpolkai T, Usher S, Stansfeld PJ & Ashcroft FM (2020*b*). New insights into KATP channel gene mutations and neonatal diabetes mellitus. *Nat Rev Endocrinol*; DOI: 10.1038/s41574-020-0351-y.

Proks P, de Wet H & Ashcroft FM (2010). Activation of the K_{ATP} channel by Mg-nucleotide interaction with SUR1. *J Gen Physiol* **136,** 389–405.

Puljung M, Vedovato N, Usher S & Ashcroft F (2019). Activation mechanism of ATP-sensitive K+ channels explored with real-time nucleotide binding ed. Kuriyan J, Swartz KJ, Swartz KJ, Shyng S-L & Goldschen-Ohm MP. *Elife* **8,** e41103.

Puljung MC (2018). Cryo-electron microscopy structures and progress toward a dynamic understanding of KATP channels. *J Gen Physiol*; DOI: 10.1085/jgp.201711978.

Rafiq M, Flanagan SE, Patch A-M, Shields BM, Ellard S & Hattersley AT (2008). Effective Treatment With Oral Sulfonylureas in Patients With Diabetes Due to Sulfonylurea Receptor 1 (SUR1) Mutations. *Diabetes Care* **31,** 204 LP – 209.

Rorsman P & Ashcroft FM (2018). Pancreatic β-Cell Electrical Activity and Insulin Secretion: Of Mice and Men. *Physiol Rev*; DOI: 10.1152/physrev.00008.2017.

Schrodinger LLC (2015). The PyMOL Molecular Graphics System, Version 1.8.

Shyng S-L, Cukras CA, Harwood J & Nichols CG (2000). Structural Determinants of PIP2 Regulation of Inward Rectifier KATP Channels. *J Gen Physiol* **116,** 599 LP – 608.

Shyng SL & Nichols CG (1998). Membrane phospholipid control of nucleotide sensitivity of KATP channels. *Science (80-)* **282,** 1138–1141.

Van Der Spoel D, Lindahl E, Hess B, Groenhof G, Mark AE & Berendsen HJC (2005). GROMACS: Fast, flexible, and free. *J Comput Chem* **26,** 1701–1718.

Stansfeld PJ, Goose JE, Caffrey M, Carpenter EP, Parker JL, Newstead S & Sansom MS (2015). MemProtMD: Automated Insertion of Membrane Protein Structures into Explicit Lipid Membranes. *Struct England1993)* **23,** 1350–1361.

Stansfeld PJ, Hopkinson R, Ashcroft FM & Sansom MSP (2009). PIP2-binding site in Kir channels: Definition by multiscale biomolecular simulations. *Biochemistry* **48,** 10926–10933.

Stansfeld PJ & Sansom MSP (2011). From coarse grained to atomistic: A serial multiscale approach to membrane protein simulations. *J Chem Theory Comput* **7,** 1157–1166.

Theobald DL (2005). Rapid calculation of RMSDs using a quaternion-based characteristic polynomial. *Acta Crystallogr Sect A* **61,** 478–480.

Trapp S, Proks P, Tucker SJ & Ashcroft FM (1998). Molecular Analysis of ATP-sensitive K Channel Gating and Implications for Channel Inhibition by ATP. *J Gen Physiol* **112,** 333 LP – 349.

Trapp S, Tucker SJ & Ashcroft FM (1997). Activation and inhibition of K-ATP currents by guanine nucleotides is mediated by different channel subunits. *Proc Natl Acad Sci* **94,** 8872 LP – 8877.

Tucker SJ, Gribble FM, Proks P, Trapp S, Ryder TJ, Haug T, Reimann F & Ashcroft FM (1998). Molecular determinants of KATP channel inhibition by ATP. *EMBO J* **17,** 3290–3296.

Tucker SJ, Gribble FM, Zhao C, Trapp S & Ashcroft FM (1997). Truncation of Kir6.2 produces ATP-sensitive K+ channels in the absence of the sulphonylurea receptor. *Nature* **387,** 179–183.

Usher SG, Ashcroft FM & Puljung MC (2020). Nucleotide inhibition of the pancreatic ATP-sensitive K+ channel explored with patch-clamp fluorometry ed. Yellen G & Aldrich RW. *Elife* **9,** e52775.

Whorton MR & MacKinnon R (2011). Crystal structure of the mammalian GIRK2 K+ channel and gating regulation by G proteins, PIP2, and sodium. *Cell* **477,** 199–208.

Wu J-X, Ding D, Wang M, Kang Y, Zeng X & Chen L (2018). Ligand binding and conformational changes of SUR1 subunit in pancreatic ATP-sensitive potassium channels. *Protein Cell* **9,** 553–567.

Yan F-F, Lin Y-W, MacMullen C, Ganguly A, Stanley CA & Shyng S-L (2007). Congenital hyperinsulinism associated ABCC8 mutations that cause defective trafficking of ATP-sensitive K+ channels: identification and rescue. *Diabetes* **56,** 2339–2348.

Zhang M, Chen X, Shen S, Li T, Chen L, Hu M, Cao L, Cheng R, Zhao Z & Luo F (2015). Sulfonylurea in the treatment of neonatal diabetes mellitus children with heterogeneous genetic backgrounds. *J Pediatr Endocrinol Metab* **28,** 877–884.

Zhao C & MacKinnon R (2021). Molecular structure of an open human KATP channel. *Proc Natl Acad Sci* **118,** e2112267118.

Figure 1

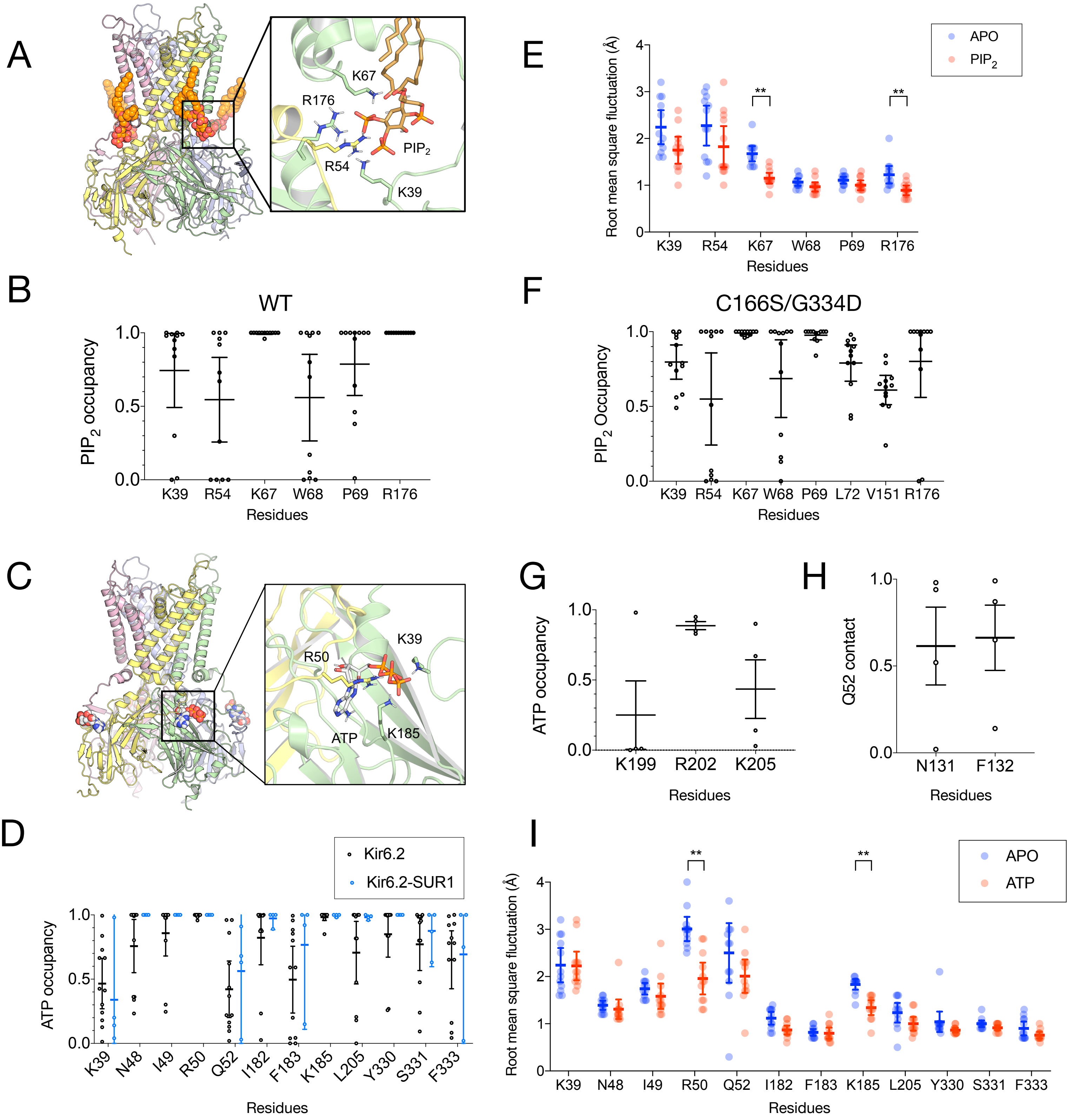
A
K67
R176
PIP$_2$
R54
K39
B
WT
PIP$_2$ occupancy
1.0
0.5
0.0
K39 R54 K67 W68 P69 R176
Residues
C
K39
R50
ATP
K185
D
Kir6.2
Kir6.2-SUR1
ATP occupancy
1.0
0.5
0.0
K39 N48 I49 R50 Q52 I182 F183 K185 L205 Y330 S331 F333
Residues
E
APO
PIP$_2$
Root mean square fluctuation (Å)
4
3
2
1
0
**
**
K39 R54 K67 W68 P69 R176
Residues
F
C166S/G334D
PIP$_2$ Occupancy
1.0
0.5
0.0
K39 R54 K67 W68 P69 L72 V151 R176
Residues
G
ATP occupancy
1.0
0.5
0.0
K199 R202 K205
Residues
H
Q52 contact
1.0
0.5
0.0
N131 F132
Residues
I
APO
ATP
Root mean square fluctuation (Å)
4
3
2
1
0
**
**
K39 N48 I49 R50 Q52 I182 F183 K185 L205 Y330 S331 F333
Residues

Figure 2

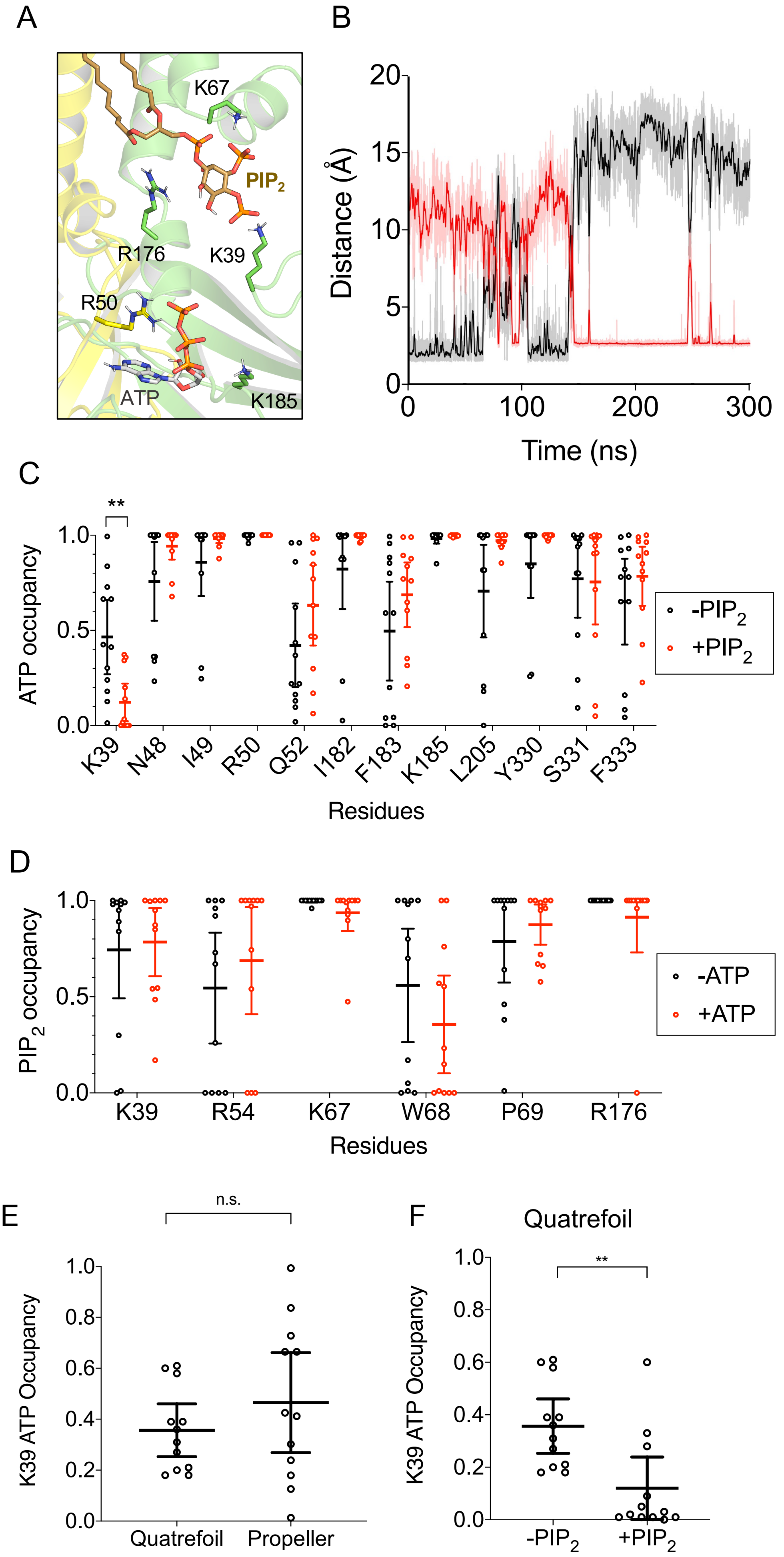
A
K67
PIP$_2$
R176
K39
R50
ATP
K185
B
Distance (Å)
20
15
10
5
0
0
100
200
300
Time (ns)
C
**
ATP occupancy
1.0
0.5
0.0
K39
N48
I49
R50
Q52
I182
F183
K185
L205
Y330
S331
F333
Residues
-PIP$_2$
+PIP$_2$
D
PIP$_2$ occupancy
1.0
0.5
0.0
K39
R54
K67
W68
P69
R176
Residues
-ATP
+ATP
E
n.s.
K39 ATP Occupancy
1.0
0.8
0.6
0.4
0.2
0.0
Quatrefoil
Propeller
F
Quatrefoil
**
K39 ATP Occupancy
1.0
0.8
0.6
0.4
0.2
0.0
-PIP$_2$
+PIP$_2$

Figure 3

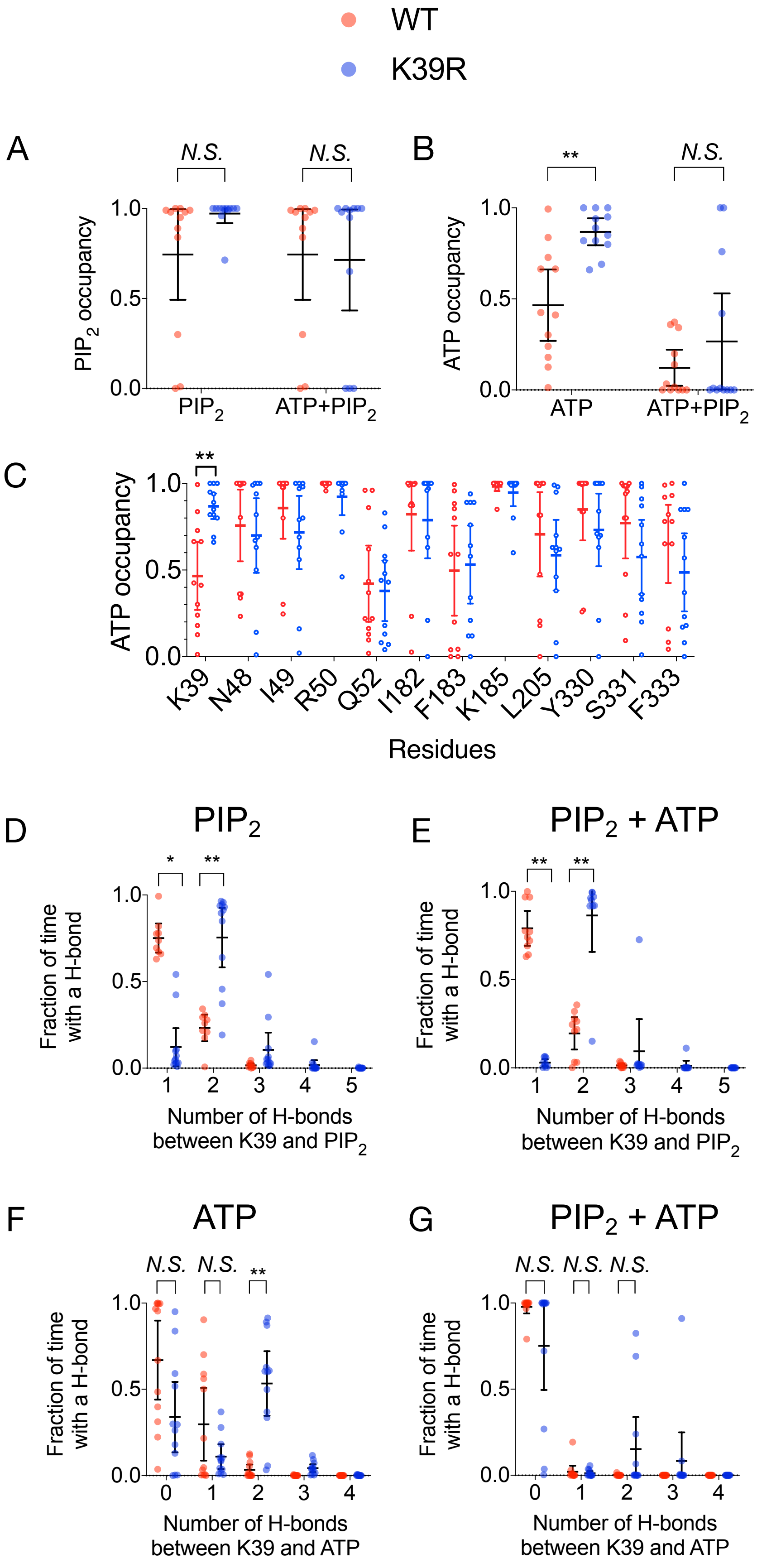
WT
K39R
A
N.S.
N.S.
PIP$_2$ occupancy
1.0
0.5
0.0
PIP$_2$
ATP+PIP$_2$
B
**
N.S.
ATP occupancy
1.0
0.5
0.0
ATP
ATP+PIP$_2$
C
**
ATP occupancy
1.0
0.5
0.0
K39
N48
I49
R50
Q52
I182
F183
K185
L205
Y330
S331
F333
Residues
D
PIP$_2$
*
**
Fraction of time with a H-bond
1.0
0.5
0.0
1
2
3
4
5
Number of H-bonds between K39 and PIP$_2$
E
PIP$_2$ + ATP
**
**
Fraction of time with a H-bond
1.0
0.5
0.0
1
2
3
4
5
Number of H-bonds between K39 and PIP$_2$
F
ATP
N.S.
N.S.
**
Fraction of time with a H-bond
1.0
0.5
0.0
0
1
2
3
4
Number of H-bonds between K39 and ATP
G
PIP$_2$ + ATP
N.S.
N.S.
N.S.
Fraction of time with a H-bond
1.0
0.5
0.0
0
1
2
3
4
Number of H-bonds between K39 and ATP

Figure 4

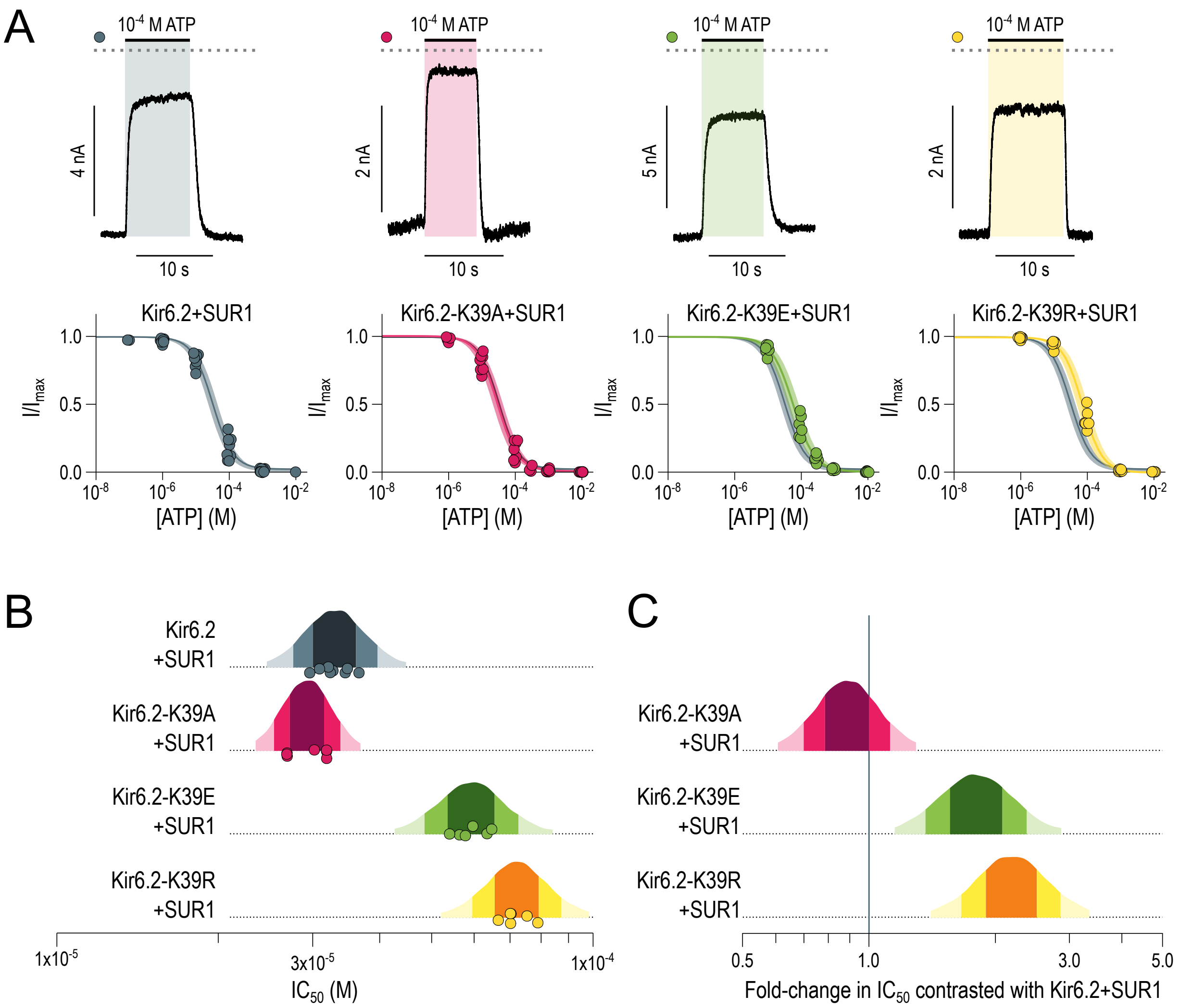
A
10-4 M ATP
4 nA
10 s
Kir6.2+SUR1
2 nA
Kir6.2-K39A+SUR1
5 nA
Kir6.2-K39E+SUR1
Kir6.2-K39R+SUR1
I/Imax
1.0
0.5
0.0
10-8
10-6
10-4
10-2
[ATP] (M)
B
Kir6.2 +SUR1
Kir6.2-K39A +SUR1
Kir6.2-K39E +SUR1
Kir6.2-K39R +SUR1
1x10-5
3x10-5
1x10-4
IC50 (M)
C
0.5
1.0
3.0
5.0
Fold-change in IC50 contrasted with Kir6.2+SUR1

Figure 5

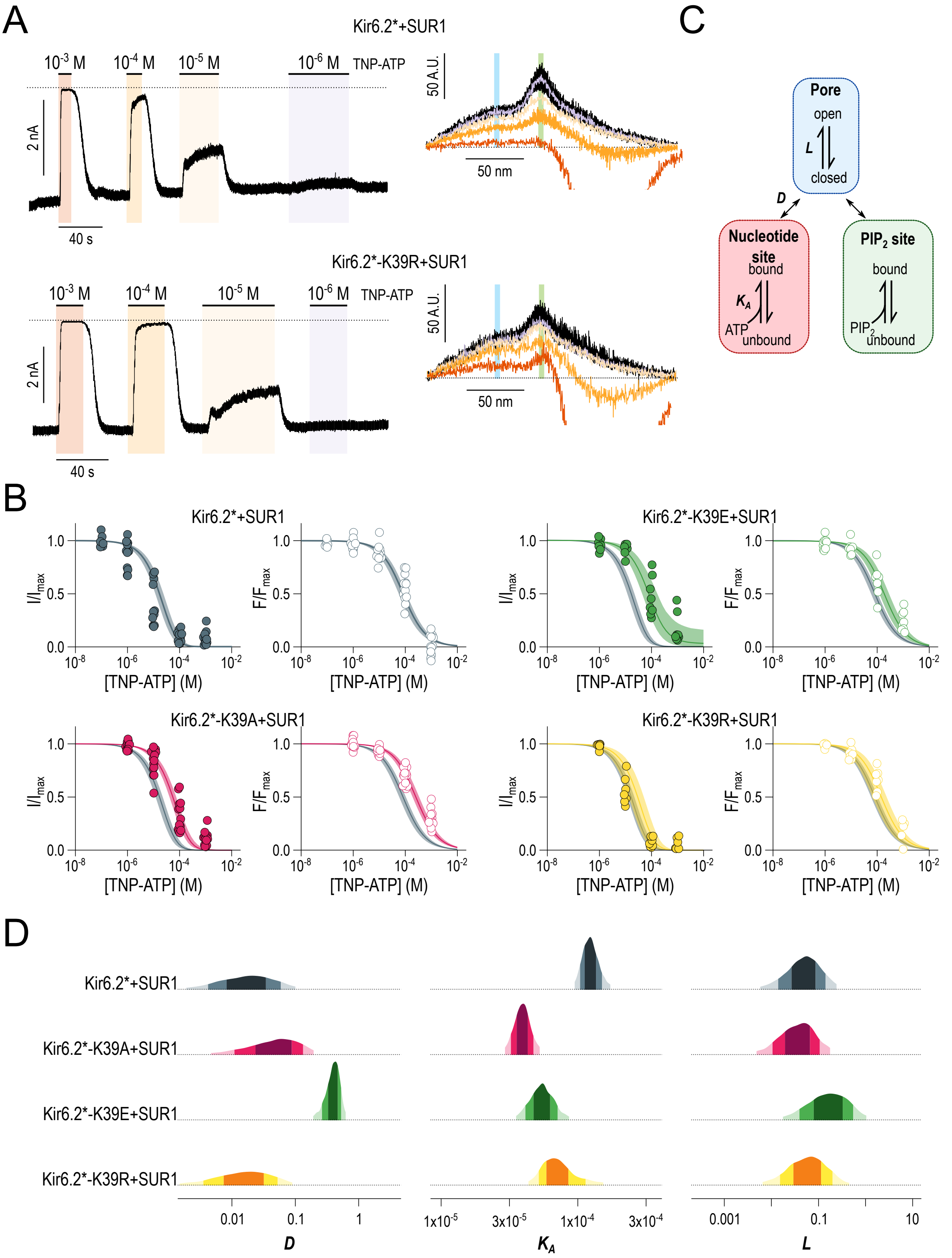
A
Kir6.2*+SUR1
10^{-3} M
10^{-4} M
10^{-5} M
10^{-6} M
TNP-ATP
2 nA
40 s
50 A.U.
50 nm
Kir6.2*-K39R+SUR1
10^{-3} M
10^{-4} M
10^{-5} M
10^{-6} M
TNP-ATP
2 nA
40 s
50 A.U.
50 nm
C
Pore
open
L
closed
D
Nucleotide site
bound
K_A
ATP
unbound
PIP$_2$ site
bound
PIP$_2$
unbound
B
Kir6.2*+SUR1
Kir6.2*-K39E+SUR1
Kir6.2*-K39A+SUR1
Kir6.2*-K39R+SUR1
I/I_{max}
F/F_{max}
1.0
0.5
0.0
10^{-8}
10^{-6}
10^{-4}
10^{-2}
[TNP-ATP] (M)
D
Kir6.2*+SUR1
Kir6.2*-K39A+SUR1
Kir6.2*-K39E+SUR1
Kir6.2*-K39R+SUR1
0.01
0.1
1
D
1x10^{-5}
3x10^{-5}
1x10^{-4}
3x10^{-4}
K_A
0.001
0.1
10
L

Figure 6

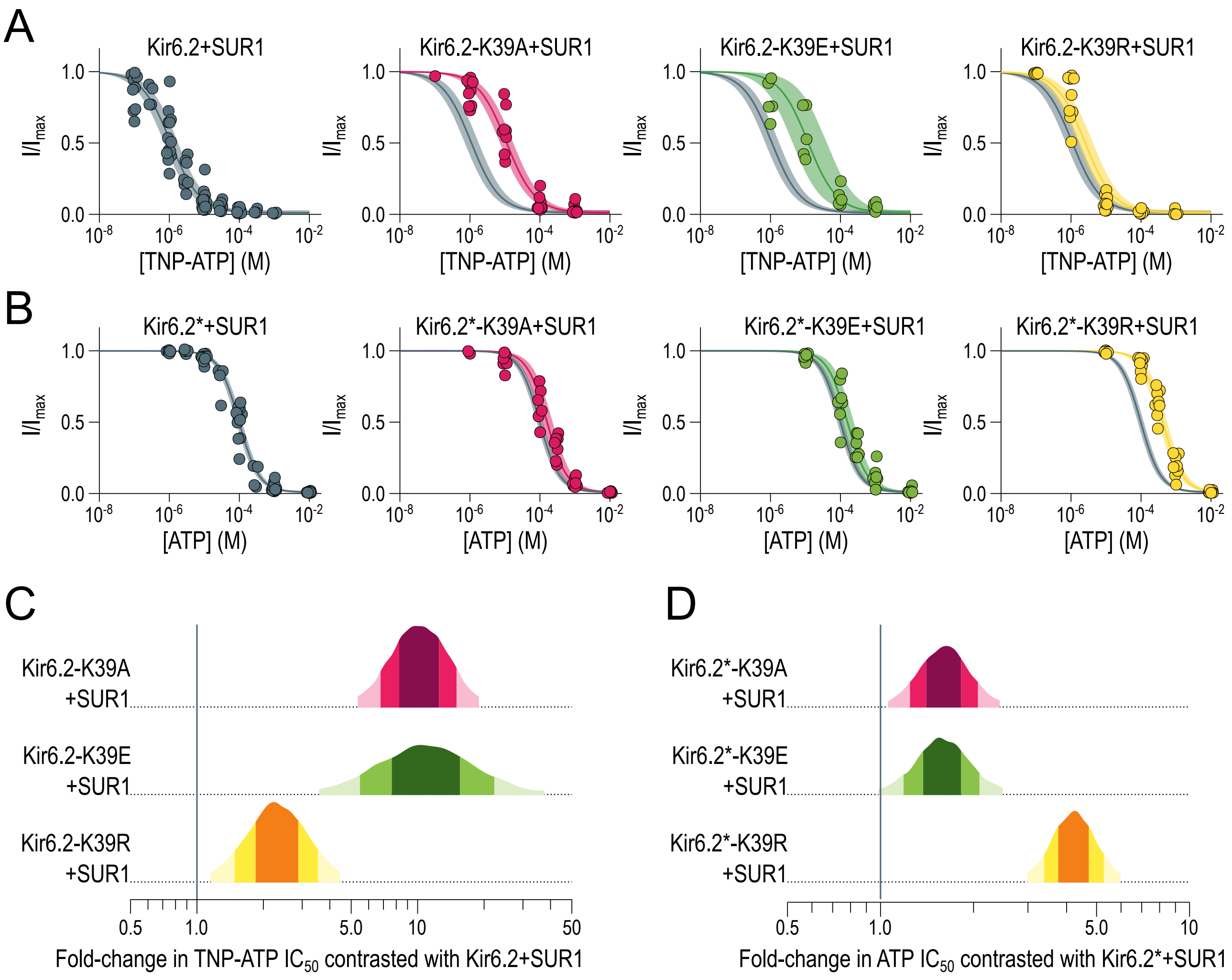
A
Kir6.2+SUR1
Kir6.2-K39A+SUR1
Kir6.2-K39E+SUR1
Kir6.2-K39R+SUR1
I/I_max
1.0
0.5
0.0
10^-8
10^-6
10^-4
10^-2
[TNP-ATP] (M)
B
Kir6.2*+SUR1
Kir6.2*-K39A+SUR1
Kir6.2*-K39E+SUR1
Kir6.2*-K39R+SUR1
[ATP] (M)
C
Kir6.2-K39A +SUR1
Kir6.2-K39E +SUR1
Kir6.2-K39R +SUR1
0.5
1.0
5.0
10
50
Fold-change in TNP-ATP IC50 contrasted with Kir6.2+SUR1
D
Kir6.2*-K39A +SUR1
Kir6.2*-K39E +SUR1
Kir6.2*-K39R +SUR1
0.5
1.0
5.0
10
Fold-change in ATP IC50 contrasted with Kir6.2*+SUR1

Figure 7

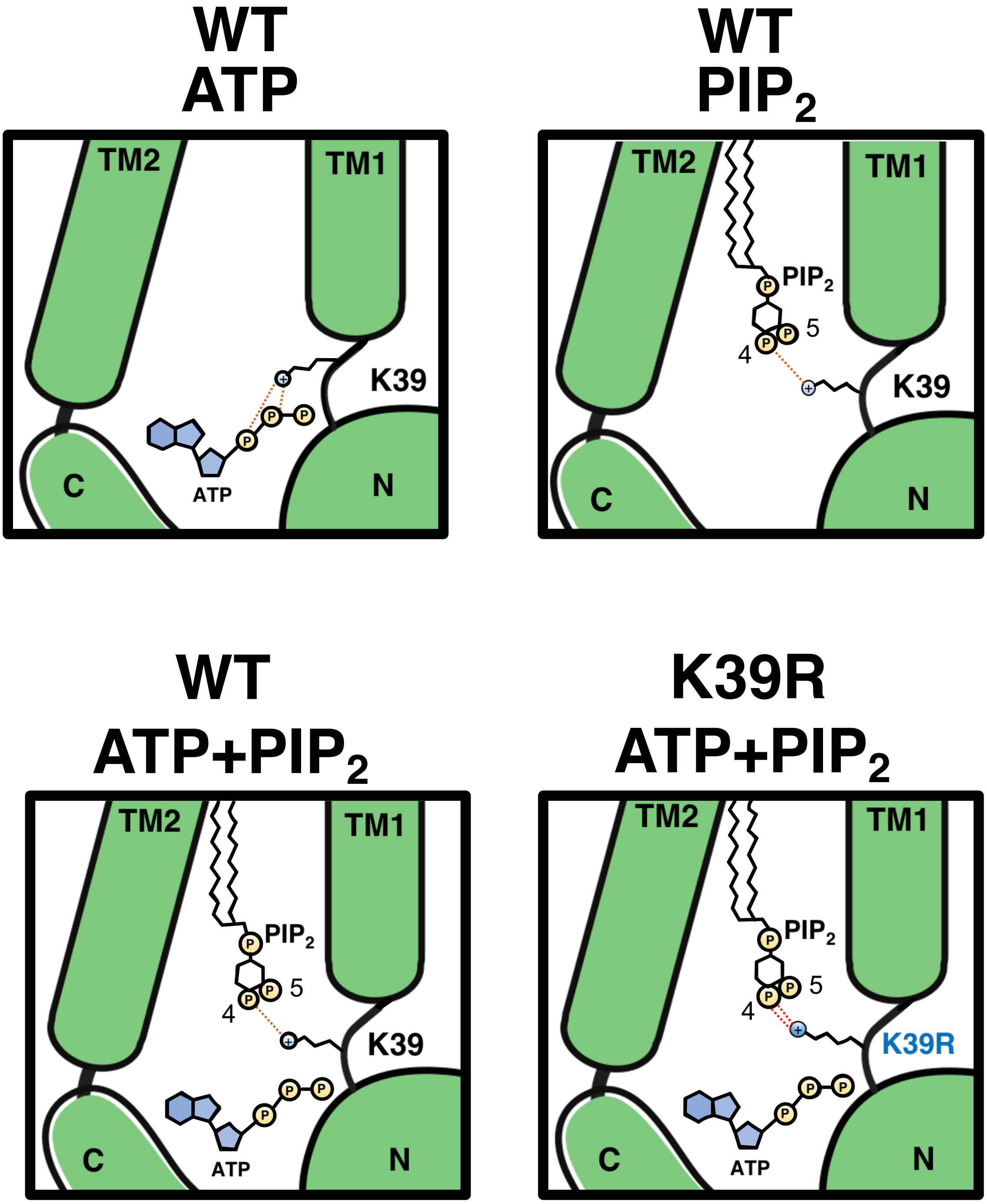
WT
ATP
TM2
TM1
K39
P
P
P
ATP
C
N
WT
PIP2
TM2
TM1
PIP2
P
P
P
5
4
K39
C
N
WT
ATP+PIP2
TM2
TM1
PIP2
P
P
P
5
4
K39
P
P
P
ATP
C
N
K39R
ATP+PIP2
TM2
TM1
PIP2
P
P
P
5
4
K39R
P
P
P
ATP
C
N